

# We are IntechOpen, the world's leading publisher of Open Access books Built by scientists, for scientists

6,000

Open access books available

148,000

International authors and editors

185M

Downloads

Our authors are among the

154

Countries delivered to

TOP 1%

most cited scientists

12.2%

Contributors from top 500 universities



WEB OF SCIENCE™

Selection of our books indexed in the Book Citation Index  
in Web of Science™ Core Collection (BKCI)

Interested in publishing with us?  
Contact [book.department@intechopen.com](mailto:book.department@intechopen.com)

Numbers displayed above are based on latest data collected.  
For more information visit [www.intechopen.com](http://www.intechopen.com)



Chapter

# Ablation of Materials Using Femtosecond Lasers and Electron Beams

*Mehra S. Sidhu and Nitish Dhingra*

## Abstract

The advancements in producing interactions of concentrated energy fluxes, such as femtosecond lasers and high-energy electron beams with the absorbing substances, have facilitated new discoveries and excitement in various scientific and technological areas. Since their invention, significant improvements in temporal, spatial, energetic, and spectroscopic characteristics have been realized. Due to the ultrashort pulse width and higher intensity ( $10^{12}$  W/cm<sup>2</sup>), it is possible to ablate the materials with negligible damage outside the focal volume, thereby allowing the treatment of biological samples, such as live cells, membranes, and removal of thin films, as well as bulk materials for many applications in diverse fields, including micro-optics, electronics, and even biology under extremely high precision. Since most biological systems are transparent toward the NIR spectral range, it follows the nonlinear multi-photon absorption interaction mechanism. In contrast, the electron beam follows linear absorption mechanism for material modifications even at lower energies. For realizing the fs-laser nano-processing in material applications, such as silicon microchips, or in biology like retinal cells, it is crucial to find a way to deliver these pulses precisely at the site of action and enhance the selectivity. The utilization of electron beams in material modification has also been exercised widely to attain nanoscale precision. In the next section, biological materials, such as cornea, retina, and silk, are discussed.

**Keywords:** ablation, biosensors, electron beams, femtosecond lasers,, nano-processing

## 1. Introduction

Ablation could be defined as the removal of material from the surface of an object by concentrated energy fluxes, such as femtosecond lasers and high-energy electron beams, by vaporization, or other erosive processes. It is a complex phenomenon that occurs upon reaching a specific energy threshold that causes measurable damage and material removal from a surface.

Surface modification of materials and devices is important for many applications, such as enhancing biocompatibility [1], promoting adhesion [2], improving wear resistance [3], preventing corrosion [4], providing hydrophilicity, hydrophobicity and electrical insulation or conducting properties, and generating antimicrobial and

antibacterial surfaces [5, 6]. Considerable advancements have been made in developing new surface modification techniques. This chapter is focused on the laser ablation (LA) and electron beam ablation (EBA) techniques, which are quite popular for material ablation. The first part of this chapter discusses the details of the LA technique, whereas the latter part is focused on the EBA technique.

The ablation threshold,  $F_{th}$  ( $J/cm^2$ ), indicates the minimum radiant exposure required to achieve effective ablative material removal. Meanwhile, the threshold fluence determines the possible precision of laser effects used for ablation and the etching of materials [7]. A low ablation threshold is generally favorable for irradiating a material with an ultrafast laser pulse to minimize the possible photo-induced damage close to the ablation area [8]. Irradiation by an intense ultrafast laser beam results in multi-photon excitation of a target material. Perhaps, the absorbed energy is transported to the electrons without thermal diffusion to the surrounding material because of the shorter pulse width of the incident pulse in comparison to the vibrational relaxation time constant of several picoseconds. As a result, thermal damage to the adjacent tissues could be minimized, and the biological tissue remains unaffected by the subsequent photo-induced mechanical shock process. This makes fs laser-assisted surgical processes non-thermal. In the vicinity of focus, the formation of a high density of free electrons could result in a local plasma formation in the targeted materials. This hot plasma formation results in permanent removal of material, even inside a cell within a sub-micron size [9].

Before discussing the details of laser ablation, it is imperative to discuss pulsed-laser interactions with biomaterials. The biomaterials discussed here, are the materials having low thermal/electrical conductivity and no free electrons. Common materials, such as fused silica, sapphire, bone, retina, silk, cornea, heart-tissue, and fall under this category [10]. In the next section, biological materials, such as cornea, retina, and silk, are discussed.

## **2. Laser interactions with biomaterials**

The interaction of light with matter can occur through several different nonlinear processes, such as two-photon or multi-photon absorption, second harmonic generation, or Raman scattering. It is useful in deep-tissue two-photon imaging. Moreover, if irradiance is high enough, any material can be machined to very high precision by using ultrashort laser pulses. This interaction is independent of linear absorption properties of the materials and which would otherwise be transparent to the laser wavelength. Ablations to micron scale precision with minimal collateral damage to the rest of the material are achieved by faster removal of material than the rate of heat conduction to the bulk.

In present clinical practices, pulses longer than a few tens of picoseconds have been utilized. It can cause damage to the dielectrics involving heating of seed electrons and transfer of this energy to the lattice. This damage occurs via conventional thermal deposition resulting in the melting and boiling of dielectric material (**Figure 1(a)** and **(b)**). Because the energy is transferred through thermal conduction, this model predicts a square root ( $\tau^{1/2}$ ) dependence of the threshold fluence ( $F_{th}$ ; energy/area) upon pulse duration ( $\tau$ ) (**Figure 2**) [13].

With these conventional lasers, the material is removed by thermal ablation, wherein the material is locally heated to near the boiling point. Since the boiling point of dielectrics is very high  $\sim$ typically  $1000^\circ\text{C}$ , this ablation is coupled with a strong

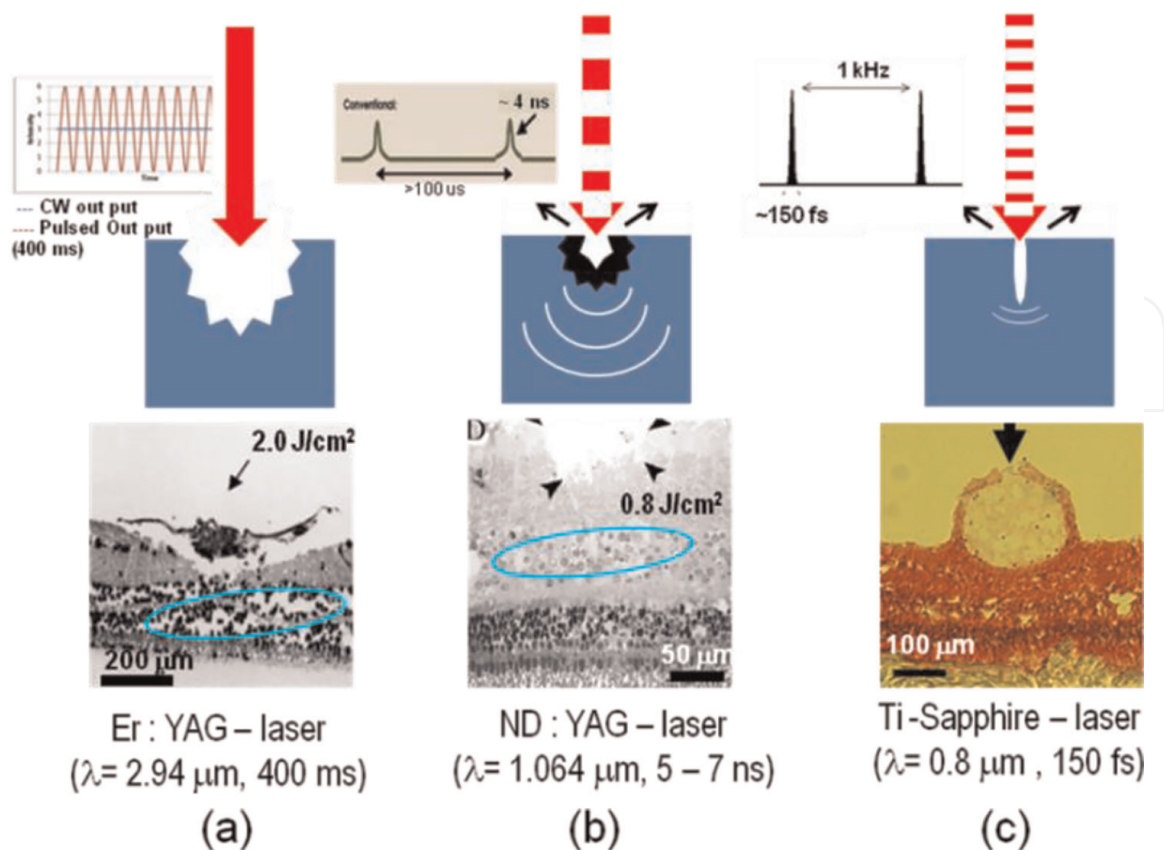


**Figure 1.** (a) Ablations of retinal-tissue with 2.94  $\mu\text{m}$  millisecond pulses ( $2 \text{ J/cm}^2$ , 400 ms), (b) retinal ablations with 1.064  $\mu\text{m}$  nanosecond pulses ( $0.8 \text{ J/cm}^2$ , 5–7 ns), and (c) retinal blood vessel ablation with 0.8  $\mu\text{m}$  femtosecond pulses (150 fs) [11, 12].

thermal shock transferred to the adjacent material. This thermal shock often results in cracking of the adjacent material in an uncontrolled manner. These effects can be observed in **Figure 1(a)** and **(b)**, where the ablations of porcine retina using a conventional Er:YAG ( $\lambda = 2.94 \mu\text{m}$ ) and ND:YAG laser ( $\lambda = 1.064 \mu\text{m}$ ) are shown [11, 12]. Meanwhile, fs-pulses (800 nm) having sufficient intensity for multi-photon ionization throughout its beam waist ablate the retinal vessel walls in an extremely controlled manner (**Figure 1(c)**). The heat transfer into the surrounding material was minimal and also no thermal shock-induced cracking was observed. It could be inferred that the laser damage threshold for dielectrics with lasers having pulse durations less than a few picoseconds to femtosecond does not follow the proportionality rule of square dependence [14–16]. In the next section, various ionization mechanisms operating in biological materials are briefly discussed.

### 3. Mechanism of ionizations

The changes in surface morphology and deviation from the  $\tau^{1/2}$  dependence of the damage threshold on pulse duration are predicted by a rapid ionization mechanism. As shown in **Figure 4**, field-induced multi-photon ionization produces free electrons that are then rapidly accelerated by the laser pulse. This could be further described as avalanche ionization and tunnel ionization. As shown in **Figure 3**, by absorbing the incident photons, the kinetic energy of a free electron becomes sufficiently high and a

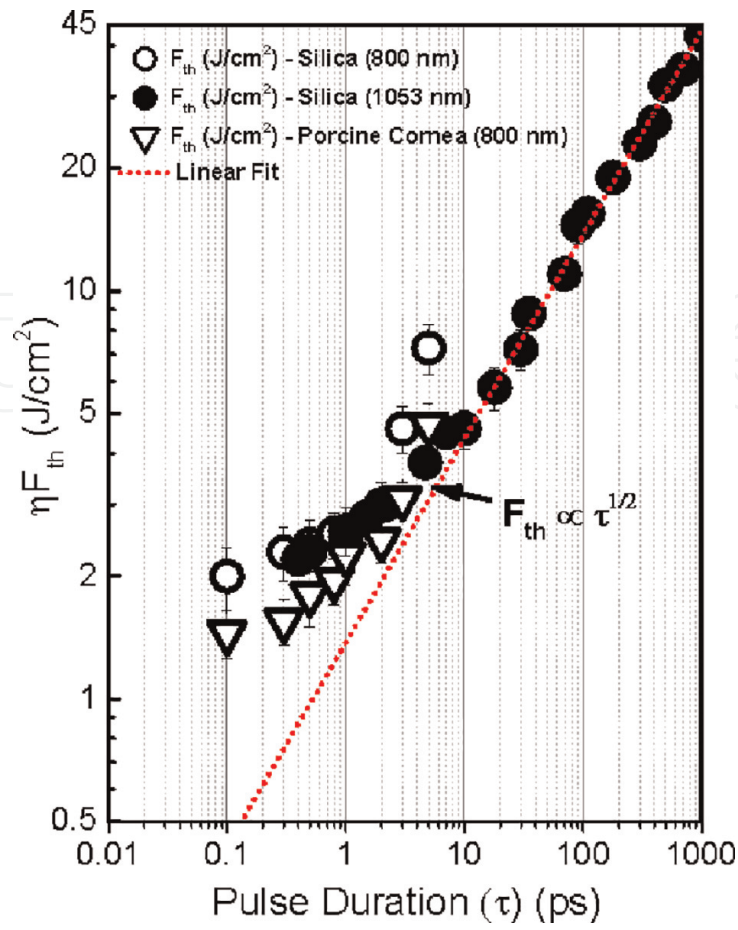


**Figure 2.** Threshold dependence on incident energy density on laser pulse duration. A square root dependence is postulated for pulse durations between picoseconds and microseconds. The parameter is tissue-dependent and is expressed in J/cm<sup>2</sup> [13].

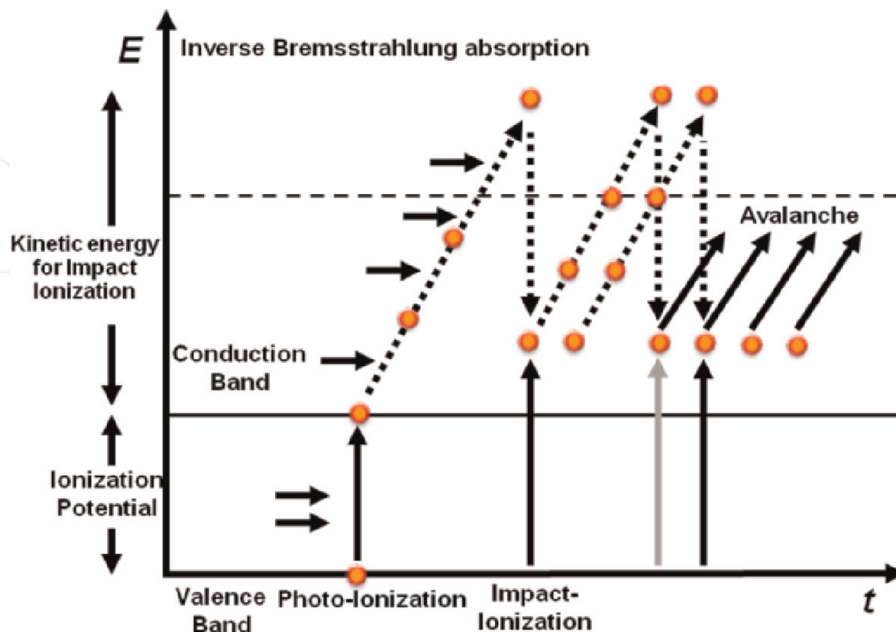


**Figure 3.** Interplay of photo-ionization, inverse bremsstrahlung absorption, and impact ionization in the process of plasma formation. Recurring sequences of inverse bremsstrahlung absorption events and impact ionization lead to an avalanche growth in the number of free electrons [19].

part of the energy may be transferred to the bound electrons by collisions to overcome the ionization potential, and hence, produce two free electrons. This is referred to as “collisional impact ionization” [16, 19–22]. Subsequently, the free electrons absorb photons and produce more free electrons from the bound electrons. Such a series of the impact ionization process is called “avalanche ionization” [16, 17]. The avalanche ionization strongly depends on free electron density and is assumed to vary linearly with the laser intensity [23]. Its efficiency is determined by competition between energy gain through *inverse bremsstrahlung absorption* and loss in energy through the phonon emission. Avalanche ionization is responsible for the ablation of wide bandgap materials at the laser intensities below  $10^{12}$  W/cm<sup>2</sup>.

When mode-locked fs-laser pulses with intensity higher than  $10^{13}$  W/cm<sup>2</sup> interacts with dielectrics, initiation of multi-photon ionization (MI) takes place. As shown in **Figure 4**, several ( $n$ ) photons with the energy  $h\nu$  having wavelength ( $\lambda$ ) coherently strike the bound electron, acting like a single photon of  $nh\nu$  (energy) at the wavelength of  $\lambda/n$ . It results in significantly higher photon flux ( $>10^{31}$  cm<sup>-2</sup> s<sup>-1</sup>) that allows a valance band electron to be freed. Meanwhile, absorbing several photons until the total energy would exceed the values of ionization potential [24, 25]. This absorption process is achieved through the meta-stable quantum state(s).

In Q-switched nanosecond laser pulses associated with low intensities, the initial process for the generation of free electrons is supposed to be thermionic emission, that is, the release of electrons due to thermal ionization. Rather, energies and temperature are usually higher in the case of Q-switched laser pulses because of the associated increment in threshold energy of ablations. Thus, laser-induced distortions with ns-pulses are often accompanied by nonionizing side effects [18].

At intensities above  $10^{12}$  W/cm<sup>2</sup>, multi-photon absorption becomes considerably strong and even the seed electrons are not required to initialize the ionization process [10, 26]. However, tunnel ionization should be considered when the intensities are higher than  $10^{15}$  W/cm<sup>2</sup>. The tunneling ionization is the process in which the strong

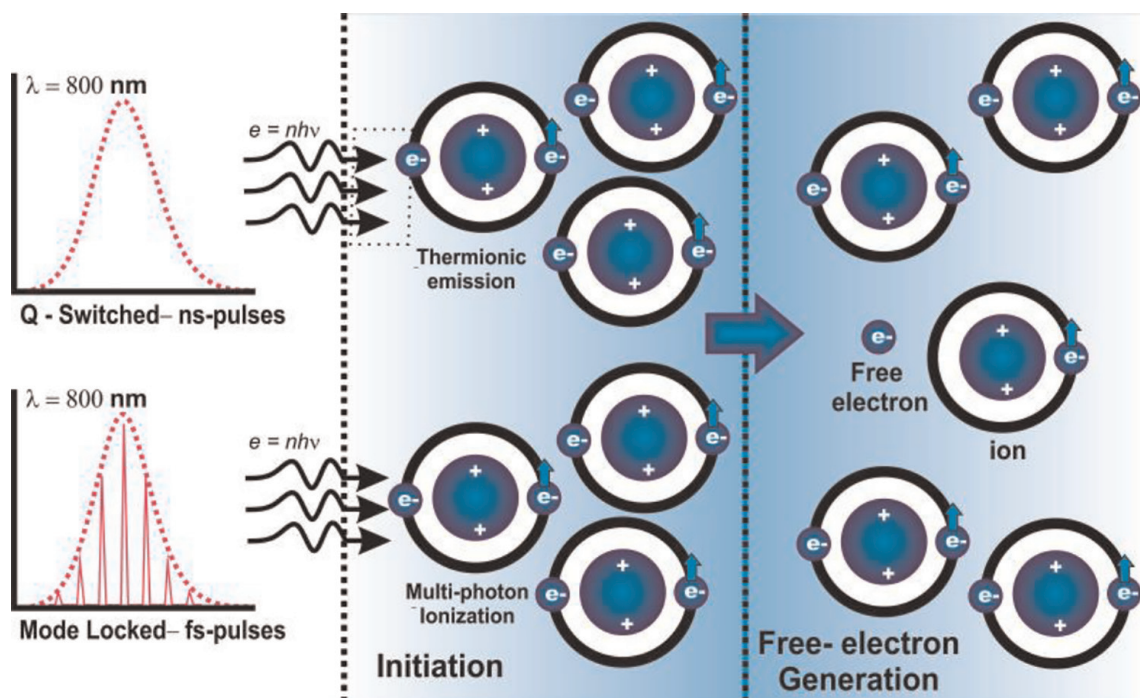


**Figure 4.**  
Schematic representation of multi-photon ionization [17, 18].

incident field suppresses the coulomb potential to allow the tunneling of a bound electron to a free state. The coulomb potential that describes the interaction between two-point charges acting along the line connecting the two charges can be expressed by the following expression;  $V_{coulomb} = q_1q_2/4\pi\epsilon_0r$ , where  $r$  is the distance between two ions,  $q_1$  and  $q_2$  represent electric charge in coulombs carried by 1 and 2, respectively, and  $\epsilon_0$  is the electrical permittivity of the space. In solids, for example, the bound electron in the valence band is excited through either multi-photon or tunneling to the conduction band and becomes quasi-free.

Keldysh developed the theory that describes the ionization of electrons in condensed matter by intense laser fields [27]. Keldysh parameter used to predict the mechanism that plays a significant role in the ionization process is defined as:

$$\gamma = \sqrt{\frac{m\omega_0^2cn_0\epsilon_0E_{gap}}{e^2I}} \quad (1)$$

where  $\omega_0$  denotes the incident laser light frequency,  $m$  is the reduced mass of the electron, and  $E_{gap}$  is the band gap of the material.  $\gamma$  can be qualitatively viewed as the ratio of the incident laser frequency and field strength ( $I$ ) [28]. For relatively weak fields with high frequencies (large  $\gamma$ ), multi-photon ionization is more important since electrons have less time to tunnel through the only moderately suppressed coulomb potential than in the small  $\gamma$  case (strong field with low frequency).

### 3.1 Laser-induced breakdown and plasma formation

When obtaining power densities of the incident laser field ( $>10^{12}$  W/cm<sup>2</sup>) is equivalent to or more than the coulomb field that binds the electron to its ionic core, the atomic coulomb force of similar magnitude was exerted on to the valence band electron and can be excited to a free state. The recurring sequence of *inverse bremsstrahlung* events and impact ionization leads to an avalanche growth in the number of free electrons. Meanwhile, the irradiance should be high enough to compensate for the losses of free electrons through diffusion out from the focus and through recombination [15, 16, 19, 20]. The energy gain at the vicinity of focus was more rapid than the energy loss by collisions with surrounding particles in media occurring without simultaneous absorption of a photon. These “cascade ionizations” in dielectrics followed by plasma formation leads to a phenomenon called *laser-induced optical breakdown* (LIOB), which can result in permanent material modification. Net free electron density is assumed to saturate at the critical density, at which modification/ablation of material takes place. For femtosecond lasers, critical density is selected as the free electron density at which plasma oscillation frequency equals to the laser frequency, and can be expressed as:

$$n_{cr} = \frac{\pi m_e c^2}{e^2 \lambda^2} \quad (2)$$

where  $m_e$  is the electron mass,  $c$  is the speed of light,  $e$  is the electron charge, and  $\lambda$  is the laser wavelength.  $n_{cr}$  is about  $10^{21}$  cm<sup>-3</sup> for 800 nm wavelength. At critical electron density, transparent dielectric materials become opaque.

#### 4. Estimation of multi-photon absorption coefficients for biomaterials

Theoretically, the multi-photon absorption is determined by the following equation,

$$\frac{dI}{dz} = \alpha_1 I + \alpha_2 I^2 + \alpha_3 I^3 + \alpha_4 I^4 + \alpha_5 I^5 \quad (3)$$

where  $I$  is the intensity of incident light beam propagating along the  $z$ -axis. The coefficients  $\alpha_1, \alpha_2, \alpha_3, \alpha_4, \alpha_5$  are one-, two-, three-, four- and five-photon absorption coefficients for a given medium, respectively. For a biomaterial, such as spider silk fiber of diameter  $D_0$ , we define the term absorption,  $A = (dI/I) (1/D_0)$ , which, using Eq. (3) becomes a polynomial of fourth-order,  $A = \alpha_1 + \alpha_2 I + \alpha_3 I^2 + \alpha_4 I^3 + \alpha_5 I^4$ . This mixed fit was used to fit the experimental data. A comparison of mixed fit with cases of pure 2-, 3-, 4-, and 5-photon absorption processes are also shown for comparison. Our fit analysis suggests that as the intensity of the pulses increases, the absorption is dominated by progressively higher-order multi-photon processes. The existence of mixed multi-photon processes for some intensity is also likely [20].

Another technique, “Z-Scan” can also be used to determine multi-photon absorption. The single silk fiber was illuminated with sub-10 fs laser beam at 85 MHz rep rate. The Rayleigh range was approximately,  $Z_R = 25 \mu\text{m}$  and the silk sample was typically  $D_0 = 1\text{--}4 \mu\text{m}$  in diameter. Thus, we satisfy the thin-sample ( $Z_R \gg D_0$ ) condition for the Z-scan measurements. The total transmission was measured by collecting the maximum light and focusing it on a photodiode, while the sample was scanned at low power and high power. The sample was translated along the beam path using a computer-controlled stage that allowed us to collect the data at about  $2 \mu\text{m}$  spacing. The normalized data for high power was obtained by subtracting the low power data to minimize any variation due to diffraction effects from silk fibers as shown in **Figure 5**. We fitted our data with the nonlinear transmission function described in Ref. [20], and reference therein. The fit function for 2-photon was,  $T_2(x) = \text{Log}(1 + C_2/(1 + x^2))/(1 + x^2)$ , with a fitting parameter  $C_2$ . The fit function for the 3-photon absorption was,  $T_3(x) = \text{Sinh}^{-1} \left[ \frac{C_3}{1+x^2} \right] / [1 + x^2]$ . The fit function for 4-photon absorption was,  $T_4[x] = \text{H2F1} \left[ 1/3, 1/3, 4/3, - \left( \frac{1 * C_4}{1+x^2} \right)^3 \right]$ , with  $C_4$  was a fit parameter. The hypergeometric function H2F1 was computed in Mathematica. Our data fitted better with 4-photon absorption fits. This was consistent with our other measurements of nonlinear transmission [20].

#### 5. Laser interaction mechanisms

On the implication of laser light into the transparent media, such as biological tissues, as well as viscoelastic like spider silk, various interaction mechanisms were facilitated. Specifically, the tissue characteristics along with the laser parameters are contributing to this diversity. Most important amongst them are optical properties of tissues that include the coefficient of reflection, absorption, and scattering. Altogether, these parameters determine the total transmission of the tissues and viscoelastic at a certain wavelength.



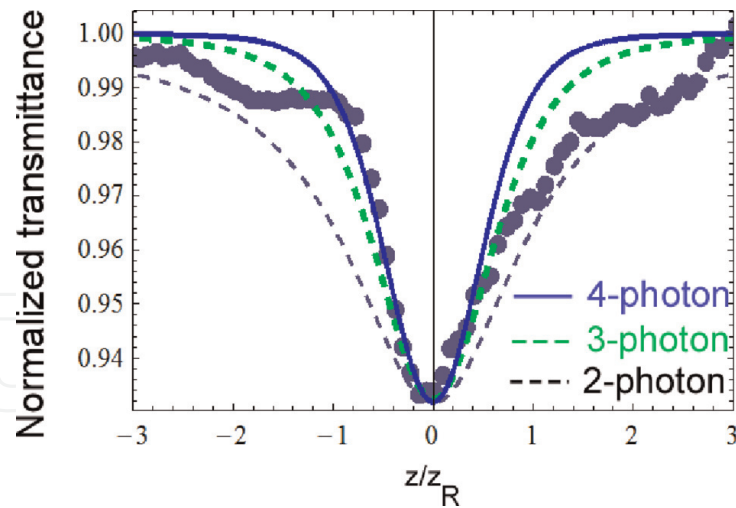


**Figure 5.** Z-scan data from a single fiber ( $\sim 150 \text{ GW/cm}^2$ ) along with equations with 2, 3, 4-photon. The mismatch near edges was attributed to diffraction losses from the edges of the silk filament. Data taken from Sidhu et al. [20].

In contrast, the following parameters that affect the laser ablation, are given by the laser radiations themselves: applied energy, wavelength, exposure time, focal spot size, and energy density. Amongst them, exposure time is a very crucial parameter when selecting a certain type of interaction.

Laser-tissue interactions can be subdivided into five different regimes depending on the laser power and the exposure time. **Figure 6** gives us a rough delineation of the interaction regimes. Two lines represented diagonally show the fluences (energy per unit area) at  $1 \text{ J/cm}^2$  and  $1000 \text{ J/cm}^2$ , respectively.

According to this plot, the time scale can be roughly divided into five parts: continuous wave or exposure times  $> 1 \text{ s}$  indicates photochemical interactions, 1 min

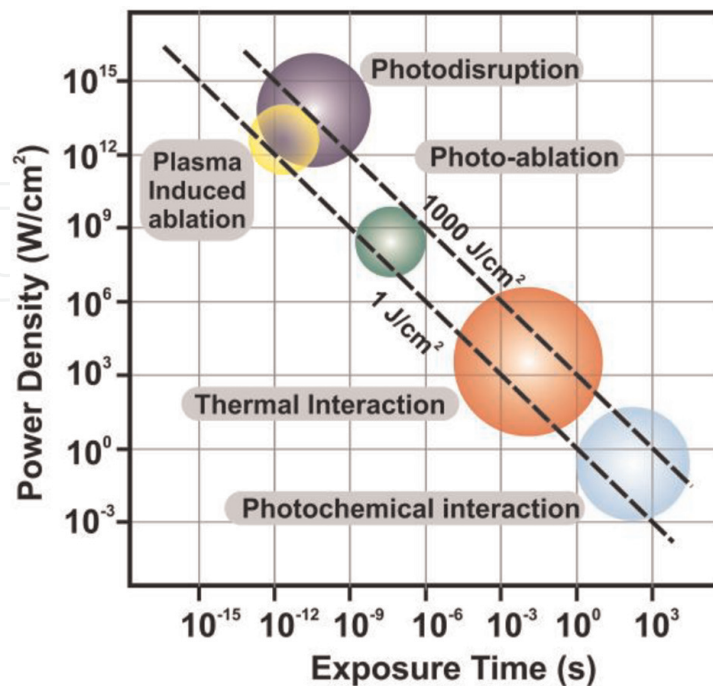


**Figure 6.** A double logarithmic map of five basic laser-tissue interactions. The circle gives only a rough estimate of the associated laser parameters [18].

down to 1 $\mu$ s indicates thermal interactions, 1  $\mu$ s down to 1 ns indicates photo-ablation, and < 1 ns indicates plasma-induced ablation, as well as photodisruption. The difference between the latter two is ascribed to different energy densities [18]. Precise laser surgery can be achieved when the desired target tissue, such as retina or ocular-tissue, is exposed to the optimal laser conditions following the subsequent interaction pathway.

### 5.1 Optical absorption and light propagation

Optical absorption takes place when the frequency of incident laser irradiation matches with an electronic excitation frequency of a molecule [18]. The typical absorption coefficient estimated by inverse Monte Carlo analysis for bovine cornea and retina at 800 nm was  $\sim 0.001 \text{ cm}^{-1}$  and  $2.5 \text{ cm}^{-1}$ , respectively [29].

The coefficients for 2, 3, 4, and 5 photon absorptions for spider silk were  $\alpha_2 = 1 \times 10^{-2} \text{ cm/GW}$ ,  $\alpha_3 = 2 \times 10^{-5} \text{ cm}^3/\text{GW}^2$ ,  $\alpha_4 = 4 \times 10^{-6} \text{ cm}_5/\text{GW}^3$ , and  $\alpha_5 = 5 \times 10^{-7} \text{ cm}^7/\text{GW}^4$ , respectively (**Figure 7**) [20, 30]. Previously, a 3-photon absorption process was observed in the silk-fibroin solution [31], and enhanced 3- and 4-photon absorption was reported for amyloid fibril solution [30].

In the case of biological tissues, such as retina and cornea-tissue, neither water nor macromolecules are present, it absorbs the light strongly in the near-infrared range (roughly between 600 to 1200 nm), this spectral range is considered a “therapeutic window.” Laser radiation in this window can penetrate deeper into biological tissues with lower loss during treatment.

Light propagation inside the retina or corneal tissues can be attributed to their absorption and scattering properties. The effective attenuation coefficient ( $A_{eff}$ ) quantifies how deep the laser light can penetrate, and is expressed as:

$$A_{eff} = \frac{1}{\sqrt{3\alpha_a(\alpha_s + (1 - g))}} \quad (4)$$

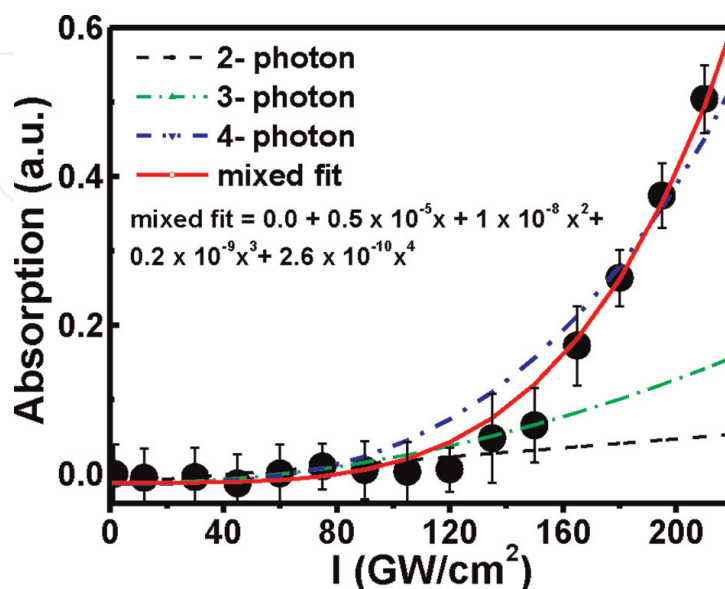


**Figure 7.** Nonlinear absorption coefficient of silk fiber versus input peak intensity. Theoretical fits for pure 2-, 3-, 4- photon absorption are compared with a mixed fit up to 4th order polynomial [20].

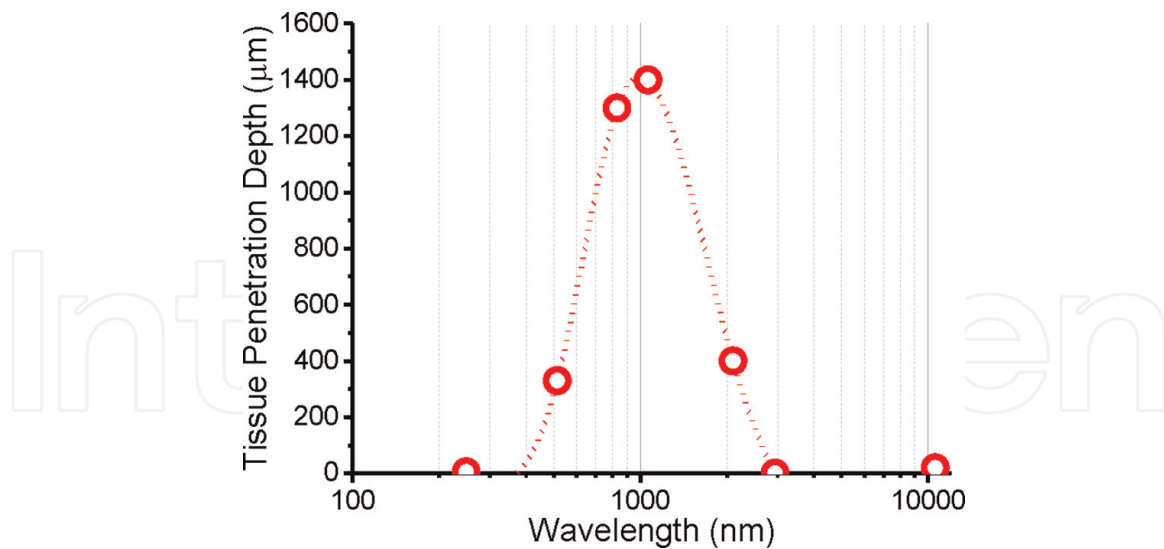


**Figure 8.** Laser penetration depth in tissue at different wavelengths [21, 27].

where  $\alpha_a$  and  $\alpha_s$  are absorption and scattering constants.  $g$  is the coefficient of anisotropy which is a tissue-dependent parameter. With  $g = 1$  denotes perfectly forward scattering, such as cornea, the effective penetration depth ( $L_{eff}$ ) of incident light is.

$$L_{eff} = \frac{1}{\alpha_{eff}} \quad (5)$$

**Figure 8** Illustrates the approximate penetration depth in tissues of different wavelengths, while both,  $\alpha_a$  and  $\alpha_s$  are taken into account.

The selection of appropriate wavelength and pulse energy followed by linear or nonlinear propagation of laser irradiations into the matched tissue target allows unprecedented precision to achieve surgical effects.

## 5.2 Photochemical interactions of fs-lasers

It is a well-known fact that light can induce chemical effects or reactions within biological tissues. In ophthalmology, photochemical interactions can play a vital role in dye-assisted photodynamic therapies (PDT). During PDT, photosensitizers were injected into the target tissues. Laser irradiations of specific wavelength trigger the photochemical reaction at low power densities ( $\sim 1 \text{ W/cm}^2$ ) and long exposure time in order of seconds to continuous wave (CW) [18, 32]. It results in toxic reaction products that cause irreversible destruction of target cell structures. The reaction could be the generation of reactive oxygen species from the interaction of light, oxygen, and photosensitizers, such as verteporfin, and indocyanine green (ICG). These were commonly used to treat choroidal or corneal neovascularization, that is, abnormal blood vessels underlying retina cell layers or sprouting in the corneal stroma, respectively. However, severe adverse reactions are associated with these photosensitizers, including visual disturbance, stromal haze, and lipid degeneration injection site reactions even after months of treatment [33]. Several joules of energy ( $\sim 150 \text{ J/cm}^2$ ) continuously deployed into corneal stroma allows long-term reduction of neovascular structure, but can also cause corneal scarring or thermal injuries [34, 35].

We suppose that without the use of chemical agents, the intensity of femtosecond laser pulses could be used to manipulate abnormal blood vessels lower than these conventional photodynamic treatment procedures. We will discuss the selective removal of corneal and retinal blood vessels in the next section of this chapter. The precise cutting and manipulation of ultrafine fibers are also discussed.

### 5.3 Thermal interactions

Thermal effects can be induced by both CW and pulsed-laser irradiations. The rise in local temperature could be attributed to the absorption of photon energy by protein, pigment, or bound water molecules. On the basis of pulse duration and peak values, different thermal effects can be achieved in tissues, including coagulation, vaporization, carbonization, and melting. Moreover, with the rise in temperature to 50°C, the enzyme activity in tissue cells is reduced, energy transfer slows down, and cell repair mechanisms are disabled. At about 60°C, protein denaturation occurs, leading to more immediate cell necrosis and tissue coagulation. Therefore, photocoagulation is the general procedure to treat retinal disease, such as proliferative diabetic retinopathy. Meanwhile, traditional lasers employed for photocoagulation (spot size: 0.1–3 mm, pulse duration: millisecond) creates a heat wave that spreads beyond the focal volume causing inevitable collateral damage to underlying cell layers [36]. This leads to scarring in the retinal segments. Thermal scarring enlarges progressively up to 300% and can cause significant vision loss if the fovea region is involved [37]. Thus, it is important to minimize the thermal effect during laser irradiations.

If pulse laser irradiations do not undergo photochemical or phase-transition processes, the linearly absorbed energy by the target tissue is entirely converted to the temperature rise. Since the focus of the current work is on femtosecond laser interaction within retinal or corneal tissues, we consider a situation where excessive laser energy, sufficiently higher than the threshold, is applied and absorbed in a small focal volume under single pulse configurations. A single shot of a fs-laser could be the entire source of heat. The temperature rise could be determined by calculating the volumetric energy density gained by the plasma during the laser pulse irradiations [38]. Under adiabatic conditions, the local temperature rise ( $\Delta T(r)$ ) at an arbitrary location ( $\mathbf{x}$ ), is directly related to the local volumetric energy density  $\varepsilon(\mathbf{x})$ , as.

$$\Delta T(\mathbf{x}) = \frac{\varepsilon(\mathbf{x})}{\rho C_v} \quad (6)$$

where  $\rho$  is the tissue density and  $C_v$  is the specific heat capacity per unit volume [19]. In case of the absence of photochemical or phase-transition, the absorbed laser energy is subjected to undergo spatial redistribution by thermal diffusion leads to collateral damage in adjacent focal volume [39]. The heated volume is a layer of tissue, where penetration length is inversely proportional to an absorption coefficient ( $1/\mu_a$ ) and the thermal diffusion time, ( $t_d$ ), is expressed as:

$$t_d = \frac{1}{\kappa \mu_a^2} \quad (7)$$

where  $\kappa$  is the thermal diffusivity. In order to achieve thermal confinement, the ratio of pulse duration ( $t_p$ ) to thermal diffusion time ( $t_d$ ) should be less than or equivalent to 1 ( $t_p/t_d \leq 1$ ). **Figure 9** shows the normalized temperature profiles in

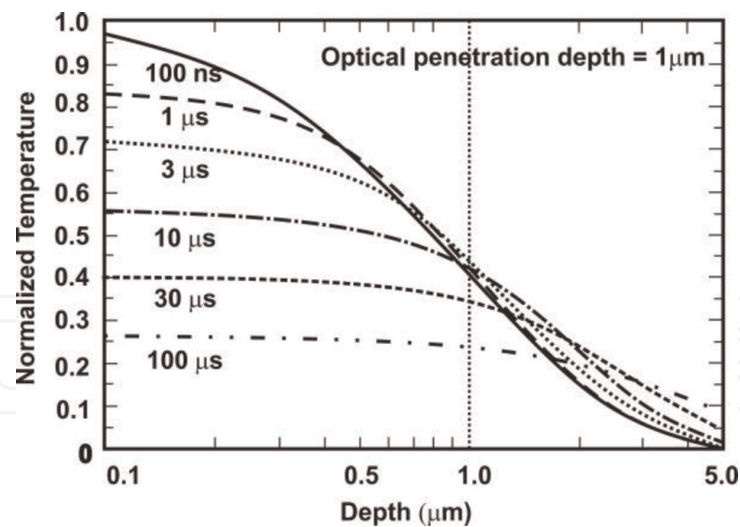


**Figure 9.** Normalized temperature profiles in water immediately after the laser irradiation with constant irradiance and optical penetration depth ( $1 \mu\text{m}$ ) at various pulse durations [19, 32].

water followed by laser irradiations with fixed radiant exposure and optical penetration depth ( $1 \mu\text{m}$ ) for various pulse durations. At typical  $t_p < 3 \mu\text{s}$ , the temperature profile is confined to the diffraction-limited volume. However, for  $t_p \geq 10 \mu\text{s}$ , the thermal diffusion has spatially redistributed the energy over the larger volume. The peak temperature also reduced significantly within the sample over time [19, 32]. Thus, pulse durations play a vital role in thermal confinement to achieve localized ablations in the target tissue.

Meanwhile, collagen fibrils and water in corneal stroma often the main chromophores contribute to the absorption of IR and UV irradiations. Collagen fibrils in corneal stroma possess microscopic tissue structures in range of  $30 \text{ nm}$  in diameter, with corresponding thermal confinement times of  $6.3 \text{ ns}$  [40]. For micro-scale thermal confinement laser pulses of picoseconds or femtosecond, duration should be employed.

#### 5.4 Plasma-induced ablation and photodisruption

Laser-induced optical breakdown occurs in biological tissues when the applied laser intensity exceeds  $10^{11} \text{ W/cm}^2$ . In case, an intense laser pulse can excite a large number of electrons and generate plasma, which causes vaporization of the materials [10–14, 18]. When a highly intense ultrashort laser pulse ( $< 10 \text{ ps}$ ) was focused into the tissue, the associated energy density is high enough to induce nonlinear absorption of laser energy through multi-photon, tunneling, and avalanche ionization [10, 16, 19, 20]. Thus, producing micrometer-sized highly excited plasma in the vicinity of the focal volume. Moreover, within the stipulated pulse duration time, the temperature of the laser-induced plasma can reach several thousand Kelvin.

During the process of optical breakdown, plasma generation allows energy deposition in pigmented, as well as weakly absorbing tissues, such as cornea, lens, or retina. Laser-induced plasma will serve as an absorber of photon energy which leads to an increment in absorption coefficient [18, 32]. Thus, by means of plasma-induced ablations, clean removal of tissue without evidence of thermal or mechanical damage can be achieved even in transparent tissues.

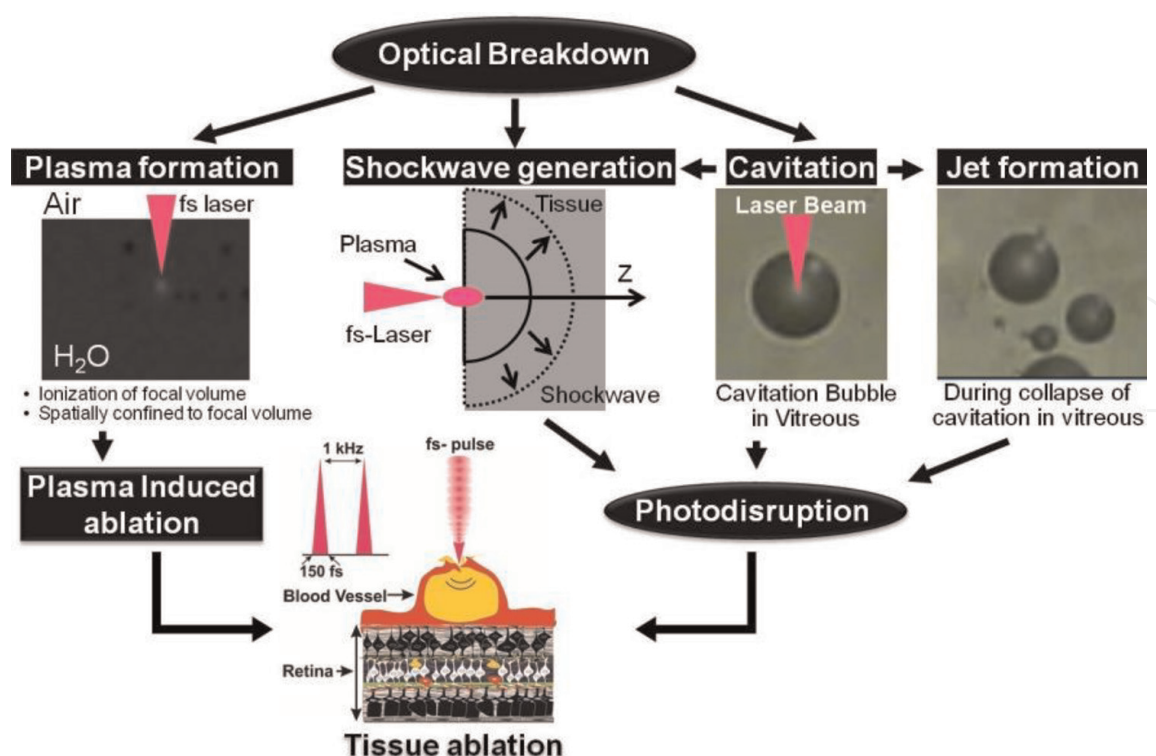


**Figure 10.** Schematic of the physical effects associated with optical breakdown [32].

Alongside plasma generation, the movement of energetic free-electrons in plasma outward from the focal volume results in secondary effects, such as shockwave generation [18, 19, 32]. The shockwave leaves the plasma boundary at supersonic velocity and then slows down to the speed of sound, refers to as acoustic wave generation. The processes associated with an optical breakdown on the interaction of fs-laser pulse with materials were shown in **Figure 10**. Lastly, if energy density still lasts at the focal volume, it forms a cavitation bubble, which performs several oscillations of expansions and collapses within a period of few hundred microseconds under external pressure [41]. **Figure 11** illustrates the scheme of physical processes associated with optical breakdown. Plasma formation followed by mechanical effects could be referred as “*photodisruption*.” It could be distinguished from plasma-induced ablations on the basis of employed laser energy density.

In plasma-induced ablations, the plasma formation vaporizes tissue at focal volume with lower threshold energies, providing a localized surgical effect. While, at higher energy densities, photo-disruption results in shock wave expansion, the expansion of the cavitation bubble, as well as heat diffusion after thermal equilibration, Thus causing all unwanted collateral damage to the surrounding tissue and limiting the surgical precision [10, 18, 19, 42, 43]. Thus, applied energy density, which is defined as energy per unit area, plays a crucial role to limit the collateral damage. The fluence ( $\text{J}/\text{cm}^2$ ) employed in the sample must be minimized while still maintaining a sufficiently higher intensity to produce photodisruption through plasma formation.

Recent studies on plasma formation in water revealed some vital trends for pulse durations dependence while inducing optical breakdown. First, on reduction of pulse duration from 100 ns to 100 fs, the irradiance threshold for breakdown increases by  $\sim 1000$  folds, but the radiant exposure threshold decreases from  $\sim 10^3$  to  $\sim 1 \text{ J}/\text{cm}^2$  [42, 43]. For nanosecond pulses, seed electrons for plasma formation

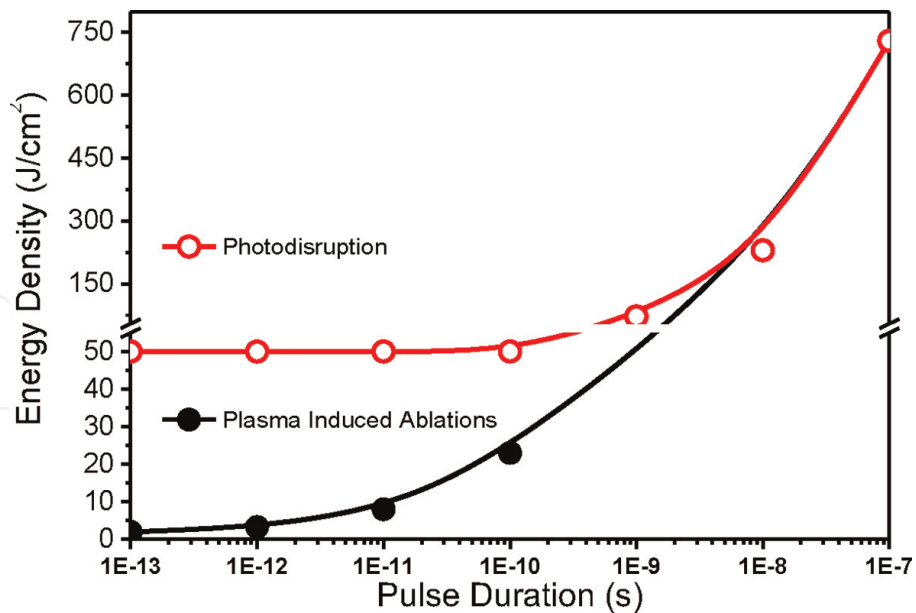


**Figure 11.** Plasma-induced ablation and photodisruption distinction on the basis of energy density in cornea tissue [32].

were generated through thermionic emission which requires higher peak intensity. Rather, higher intensity of laser field generated by picosecond and femtosecond laser pulses can cause multi-photon ionization, which supplies the seed-free electron needed to start plasma generation at much lower peak intensities. Thus, the difference in radiant exposure threshold comes from the mode of free-electron generation or the initiation of plasma generation. As a result, nanosecond pulse lasers need higher threshold energy for plasma generation as compared to femtosecond and picosecond lasers. Second, the plasma transmission is small for ns-pulses, increases considerably for picoseconds pulses with maxima around 3 ps, and decreases again for fs-pulses [43, 44]. Lastly, the plasma energy density is more than one-fold smaller with fs-pulses than with ns-pulses [42–44]. Considering the facts, fs lasers could be employed as a microsurgical tool for precise ablations of biological tissues.

## 6. Ablation of biomaterials

### 6.1 Retinal blood vessels

In this section of the chapter, the ablation thresholds for retinal blood vessels of porcine have been studied as a function of vessel wall thickness. Vessel wall thickness, as well as the lumen diameter of porcine retinal blood vessels, is gradually decreasing while moving from the optic disc to the peripheral region of the retina (**Table 1**) and it was classified as primary, secondary, tertiary, and quaternary vessels as shown in **Figure 12(a)–(e)**.

#### 6.1.1 Experimental technique

The experimental setup for fs-laser ablation of a porcine retina and as well as its blood vessels has been discussed in Ref. [45]. The laser system consists of a

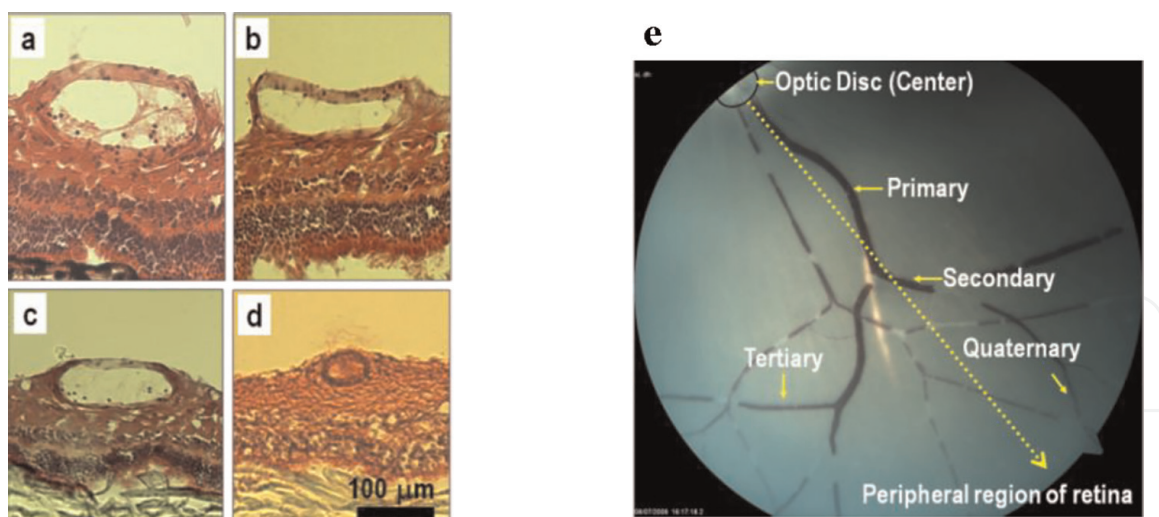


**Figure 12.** *H and E stained cryosections of retina blood vessels from the central region (optic nerve) toward the peripheral region in the porcine eye. (a) Primary (b) secondary (c) tertiary, and (d) quaternary. Scale bar is 100  $\mu\text{m}$ . (e) Fundus image of porcine retina, indicating organization of retinal blood vessels from the optic disc “center” to the peripheral region [32].*

regenerative amplified Ti: Sapphire ( $\lambda = 810 \text{ nm}$ ) laser, having a pulse width of 150-fs pulse at a repetition rate of 1 kHz (Quantronix, USA). The variable neutral density filter (Sigma, Kochi, Japan) is used for controlling the laser power. An objective lens (20X, Nikkon, Japan), was employed to focus the laser beam on the substrate surface, having a numerical aperture (N.A.) of 0.4. The diffraction-limited spot size at focus is given by.

$$D_{\min} = \frac{4\lambda}{\pi NA} \quad (8)$$

where  $\lambda$  is the wavelength (810 nm). The current optics used in this work result in a laser spot size of 2.6  $\mu\text{m}$  in diameter. In general, the actual spot size is larger than the calculated value due to discrepancies in alignment.

To estimate the vessel ablation threshold, a series of laser fluence from 0.4 to 28  $\text{J}/\text{cm}^2$  for quaternary, from 0.7 to 43  $\text{J}/\text{cm}^2$  for tertiary, from 0.7 to 71  $\text{J}/\text{cm}^2$  for secondary, and from 1.4 to 99  $\text{J}/\text{cm}^2$  for primary retinal blood vessel was employed. For 60 different porcine eyeballs, 20–25 laser treatments were conducted at periodic intervals of 100  $\mu\text{m}$  on each type of blood vessel. All the experiments were conducted under a single-shot configuration. Post-treatment of blood vessels, the histological analysis was carried out for determining the probability (%) of damage and probability (%) of vessels perforation for overlaid Inner Limiting Membrane [ILM] and the retinal blood vessels, respectively. The ILM could be defined as a thin layer membrane about  $\sim 6 \mu\text{m}$  thick over the retinal vessels. Prior to the ablation of the blood vessel lumen, ILM must be ablated [32, 46].

### 6.1.2 Laser ablations of retinal blood vessels

Femtosecond laser irradiations were employed on all four categorized blood vessels, where the threshold for ILM ablation and the vessel perforation was determined from the H & E images taken off the mapped laser lesions. Later on, the wall thickness and determining thresholds were correlated to elucidate the relationship.



| Organization level | Vessel thickness ( $\mu\text{m}$ ) | Vessel diameter ( $\mu\text{m}$ ) |
|--------------------|------------------------------------|-----------------------------------|
| Primary            | $10.01 \pm 0.28$                   | $146.12 \pm 10.55$                |
| Secondary          | $7.84 \pm 0.11$                    | $118.79 \pm 7.62$                 |
| Tertiary           | $6.64 \pm 0.71$                    | $93.11 \pm 4.93$                  |
| Quaternary         | $5.76 \pm 0.86$                    | $51.42 \pm 7.32$                  |

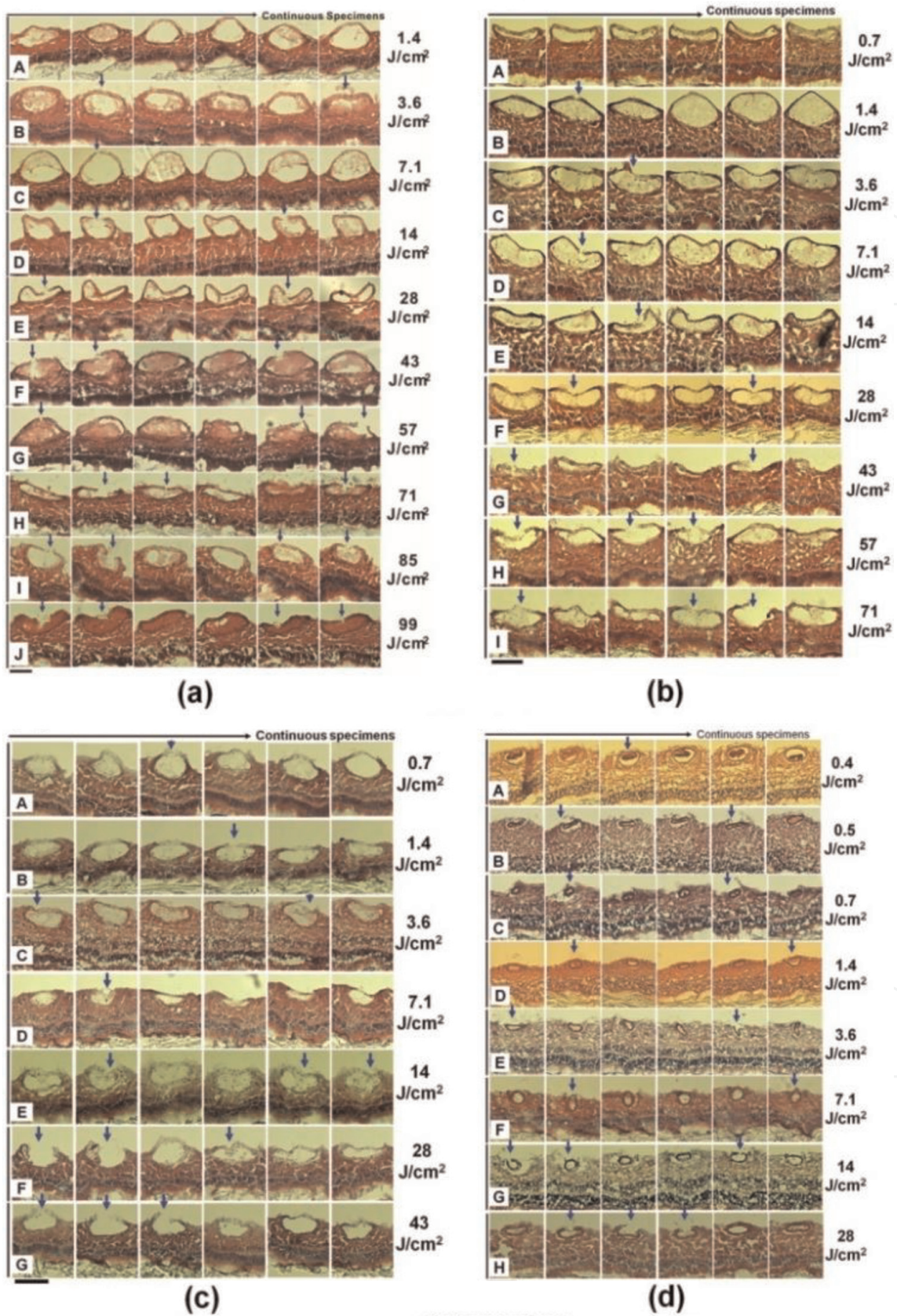
**Table 1.**  
Vessel wall thickness and lumen diameter of porcine retinal blood vessels [32].

By changing the laser fluence from  $1.4$  to  $99 \text{ J/cm}^2$ , we produce a series of lesions on the primary blood vessel walls with a single fs-laser pulse. Considering the gradual decrease in total wall thickness of secondary, tertiary, and quaternary blood vessels, the lowest fluence at which no ablations on ILM was found to be  $0.4 \text{ J/cm}^2$ . However, the fluence at which the 100% probability of vessel perforation achieved was declined with the decrease in organization hierarchy from primary ( $99 \text{ J/cm}^2$ ), secondary ( $71 \text{ J/cm}^2$ ), tertiary ( $43 \text{ J/cm}^2$ ) to quaternary ( $28 \text{ J/cm}^2$ ) level. In all levels of blood vessels, with the progressive increase in laser fluence, the probability of ablation of the ILM and the vessel perforation show a monotonic increase. **Figure 13** exhibits the histological images of the sectioned slices of vessels after successive laser irradiations (a) primary, (b) secondary (c) tertiary, and (d) quaternary. As the size of the quaternary vessels is quite small, it is difficult to locate the laser lesions on the surface of blood vessels, therefore,  $40\times$  objective is used to map the laser lesions.

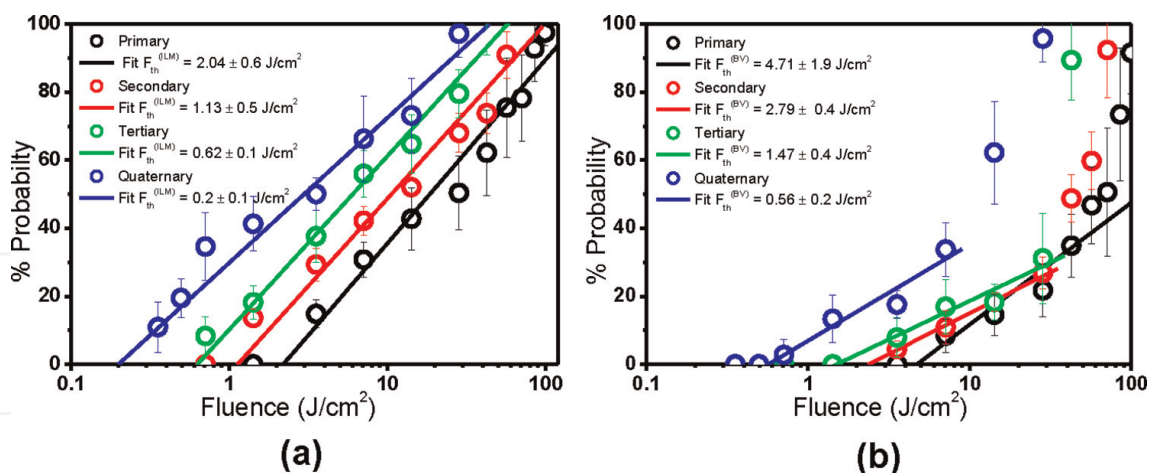
On analysis of histological sections, no apparent ablation of the ILM and no blood outflow were observed for the laser fluence less than  $1.4 \text{ J/cm}^2$  in the case of secondary and tertiary blood vessels, whereas this value was further decreased to  $0.5 \text{ J/cm}^2$  for quaternary blood vessels.

As per the analysis of cryosections, the lateral damage of the retinal blood vessels on fs-laser exposure is limited to  $20 \mu\text{m}$  range at lower laser fluences. First apparent optoperforation of secondary and tertiary blood vessels was observed at the laser fluence of  $3.6 \text{ J/cm}^2$  (**Figure 13(b)**-C and (**c**)-C), and on quaternary blood vessels it was noticed at  $0.7 \text{ J/cm}^2$ . Even though the blood vessel size is tens of micrometers, due to the precise focusing of fs-laser irradiations any damage to adjacent and underlying retinal-tissue is avoided. Meanwhile, on increasing the laser fluence to  $14 \text{ J/cm}^2$  for secondary,  $7.1 \text{ J/cm}^2$  for tertiary, and  $3.6 \text{ J/cm}^2$  for quaternary blood vessels, single-pulse laser irradiation induces complete optoperforation of the blood vessel wall.

The cryosections of the blood vessels irradiated with a single-shot ultrafast laser were grouped into three types of lesions, including no change, ablation only at the ILM, and optoperforation of blood vessel walls. On this basis, correlation statistics of these different types of lesions are shown in **Figure 14** as a function of laser fluence. The perforation probability of blood vessels increased in the fluence range of  $0.4$ – $99 \text{ J/cm}^2$ . The ablation threshold of all the blood vessels has been illustrated in **Table 2**. We determined the laser fluence to ablate the ILM layer over the blood vessels. It was found to be in the range of  $1.4$ – $3.6 \text{ J/cm}^2$  for primary,  $0.7$ – $1.4 \text{ J/cm}^2$  for secondary and tertiary, and  $0.4$ – $0.5 \text{ J/cm}^2$  for quaternary blood vessels. However, fs-laser-assisted perforation of blood vessels was achieved at higher laser fluence. Vessel perforation of secondary, tertiary, and quaternary vessels could be achieved with a fluence between  $2.5$ – $3.6 \text{ J/cm}^2$ ,  $1.4$ – $2.5 \text{ J/cm}^2$ , and  $0.5$ – $1.4 \text{ J/cm}^2$ , respectively.



**Figure 13.** Sequential H & E stained cryosections of retinal blood vessels after single fs-laser irradiations. ( $t = 20 \mu\text{m}$ ). (a) Primary (b) secondary (c) tertiary, and (d) quaternary retinal blood vessels. Overall incident laser fluence is raised from 0.4 to 99 J/cm<sup>2</sup> or until 100% vessel perforations were achieved at each organization level. Scale bar is 100  $\mu\text{m}$  [32, 46].


**Figure 14.**

(a) Linear plot of percent probability of damage for inner limiting membrane (ILM) and (b) vessel perforation as a function of the laser fluence for primary, secondary, tertiary, and quaternary blood vessels. With a progressive increase in the laser fluence, the percent probability of the blood vessel perforation shows a monotonic increase. The lines represent the extrapolation of the probability of damage to determine the ILM ablation threshold and vessel perforation threshold [32].

| Organization level | ILM ablation threshold (J/cm <sup>2</sup> ) | Vessel perforation (J/cm <sup>2</sup> ) |
|--------------------|---|---|
| Quaternary         | $0.20 \pm 0.1$                              | $0.56 \pm 0.2$                          |
| Tertiary           | $0.62 \pm 0.1$                              | $1.47 \pm 0.4$                          |
| Secondary          | $1.13 \pm 0.5$                              | $2.79 \pm 0.4$                          |
| Primary            | $2.04 \pm 0.5$                              | $4.71 \pm 1.9$                          |

**Table 2.**

ILM ablation and vessel perforation threshold for retinal blood vessels (porcine).

It is the nonlinear nature of ultrafast laser-tissue interaction that leads to the three-dimensional submicron confinement of the laser absorption below the surface. The high peak intensities of ultra-short laser pulses provide a high flux of photons that could be nonlinearly absorbed by the electrons. The ultrafast duration of the absorption process leads to a rapid and efficient plasma generation where the beam is focused. Therefore, pulse energies as minimum as a few nano-joules (nJ) are sufficient for ablation of sub-cellular structures when the beam is tightly focused to submicron size [19, 47–49].

Comparative analysis of blood vessel optoperforation thresholds and ILM ablation thresholds for various blood vessels shows an increment with the increase in the wall thickness and lumen diameter. This provides an idea to selectively operate the blood vessels while discriminating on the basis of size as well as wall thickness without any apparent collateral damage to the underlying cell layers.

### 6.1.3 Corneal vessel ablation

Near-Infrared (NIR) femtosecond (fs) laser pulses focused into a transparent cornea allow surgery on neovascular structures with minimal collateral damage following the phenomenon of nonlinear multi-photon absorption. The fundamental output from a regenerative amplified Ti-sapphire laser with  $\lambda = 810 \text{ nm}$ , having a pulse

width of 150 fs and a repetition rate of 1 kHz (Libra, Coherent Inc., USA) was focused into the rat corneal stroma by an ophthalmoscope lens (focal length = 36 mm, Carl Zeiss Inc., Germany). The numerical aperture (N.A) was 0.16. The laser spot was circular with a spot diameter of about 7.6  $\mu\text{m}$  (measured at  $1/e^2$  in intensity) [50].

The system was ingeniously made that includes a software-controlled laser aiming equipment with an xy-galvano scanner to track pre-assigned targets visualized in optical images of the rat cornea. A schematic diagram of the experimental setup is illustrated in **Figure 15**, where under anesthetic conditions, the rat body was placed on a motorized XYZ translation stage, used to manipulate the target to expose a fresh area of tissue at each laser scan.

The minimal visible laser (MVL) lesion threshold was estimated for corneal neovascularizations (*abnormal blood vessels grown under adverse conditions in the avascular cornea*) by varying the laser fluence from 2.2 to 8.6  $\text{J}/\text{cm}^2$ . The area of a scan was  $150 \times 150 \mu\text{m}$ , and the number of incident laser pulses (about 400) was kept constant [50].

The MVL lesion ablation threshold over the abnormal corneal blood vessels referred to as “neovascular structures” was estimated from high-resolution CCD images captured before and after the fs-laser exposure (**Figure 16**) Any noticeable or

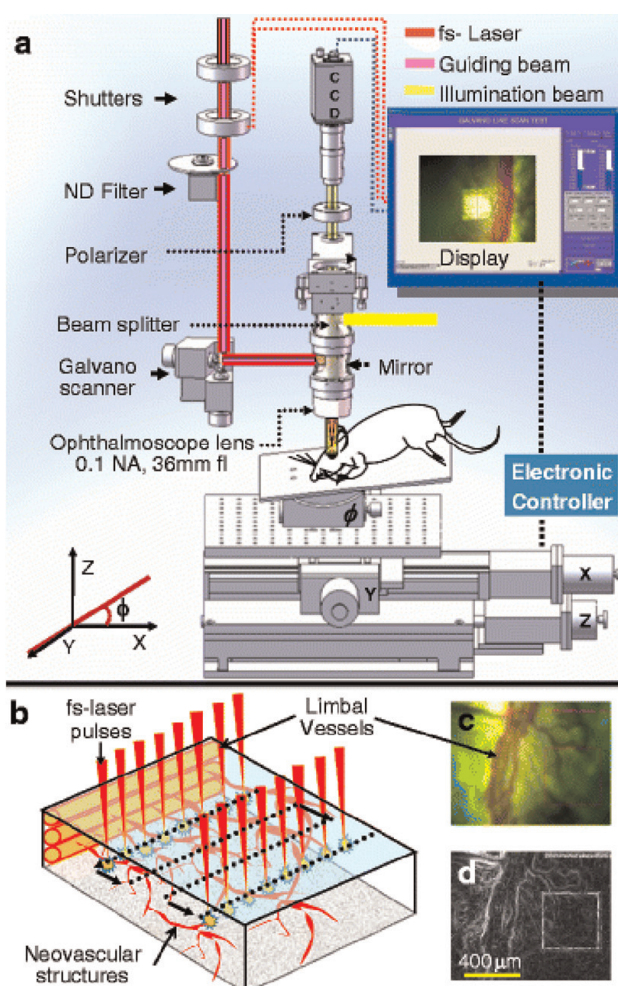


**Figure 15.** (a) Schematic diagram of fs laser-assisted corneal neovascularization treatment system. (b) Schematic representation of scanning pattern of laser pulses into the corneal stroma. (c, d) Optical and transformed image of rat cornea captured before exposure of fs laser irradiation. Scale bar is 400  $\mu\text{m}$  [50].

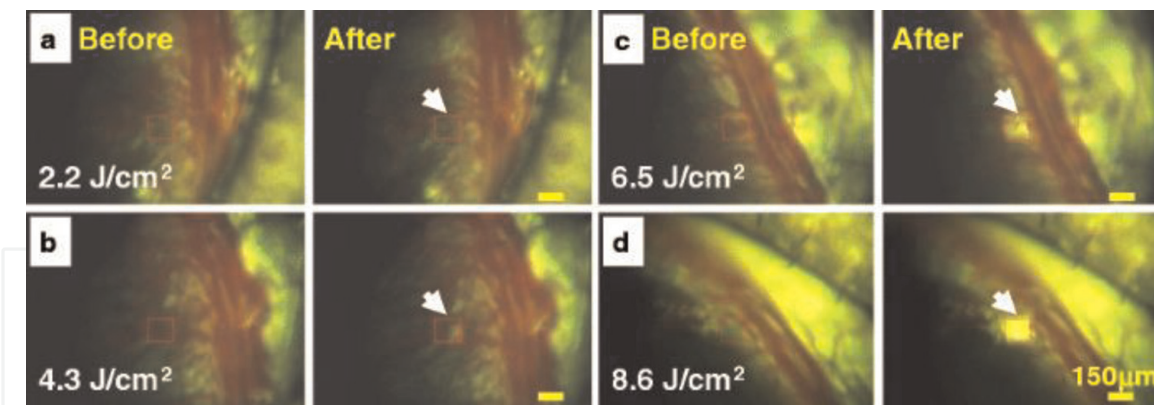


**Figure 16.** Sequential CCD images of Norway brown rat cornea before and after the exposure of fs-laser irradiation where the laser fluence is  $2.2 \text{ J/cm}^2$  (a),  $4.3 \text{ J/cm}^2$  (b),  $6.5 \text{ J/cm}^2$  (c), and  $8.6 \text{ J/cm}^2$  (d). The scan area indicated by red-colored squares is  $150 \times 150 \text{ }\mu\text{m}$ . Scale bar is  $150 \text{ }\mu\text{m}$ .

identifiable changes observed on neovascular structures under the high-resolution microscope in comparison to the neighboring intrastromal region immediately after the laser exposure were classified as an indication of damage.

At the fluence of  $4.3 \text{ J/cm}^2$ , the first visible, detectable lesion was found (**Figure 18b**) and is referred to as the minimal visible laser (MVL) lesion threshold. There was no clear damage found on either the intrastromal region or the neovascular structures at fluences  $< 2.2 \text{ J/cm}^2$ . When the set laser fluence was increased to  $6.5 \text{ J/cm}^2$  or more, the size of the lesions also increased such that it covered the entire laser scanning area. For currently used femtosecond exposures, the laser pulse duration is shorter than the electron cooling and recombination times [19, 51, 52]. Thus, the minimal energy is nonlinearly absorbed during the pulse into the focused portion of tissues. However, the time scale of absorption is much shorter than both the thermal diffusion and shockwave propagation times. This might lead to localized photodisruption effects and subsequent reduction of stromal damage within the vicinity of laser focus [19, 51, 52]. fs ultrashort pulsed lasers for enclosure of corneal neovascularization in the presence of ICG at  $3.8 \text{ J/cm}^2$  was employed by Sawa et al. in 2004 [53]. The MVL threshold values determined in the current study are in good agreement with previous reports [45, 53, 54], despite that no dye or photodynamic chemical agents were applied during the procedures.

## 6.2 Laser ablation of viscoelastic ultrathin spider silk fibers

We estimated a single-shot response of spider silk fiber of about  $2\text{--}3 \text{ }\mu\text{m}$  in diameter (**Figure 17**) [20, 55]. It is positioned at the focus using  $100\times$  objective (NA: 0.9) with an estimated beam spot size around 1 micron. SEM micrographs illustrate the single-pulse ablation of silk fiber at  $0.1 \text{ }\mu\text{J}$  and  $0.3 \text{ }\mu\text{J}$  pulse energies. The estimated ablation threshold ( $F_{\text{th}}$ ) for spider silk is about  $0.05 \text{ }\mu\text{J}$  ( $1 \text{ J/cm}^2$ ). A slightly lower ablation threshold ( $0.6 \text{ J/cm}^2$ ) for silkworm silk is reported for different laser parameters with 230 fs pulses at the central wavelength of 515 nm wavelength [56]. This could be due to differences in the laser parameters, as well as the material properties [19, 20, 57].  $F_{\text{th}}$  is found to be significantly higher than the ablation threshold for the crystalline Si, it could be attributed to the nonabsorbing nature of silk sample for incident laser wavelength, that is, 800 nm [19, 41]. By compensating for the dispersion of the fs-pulse, it

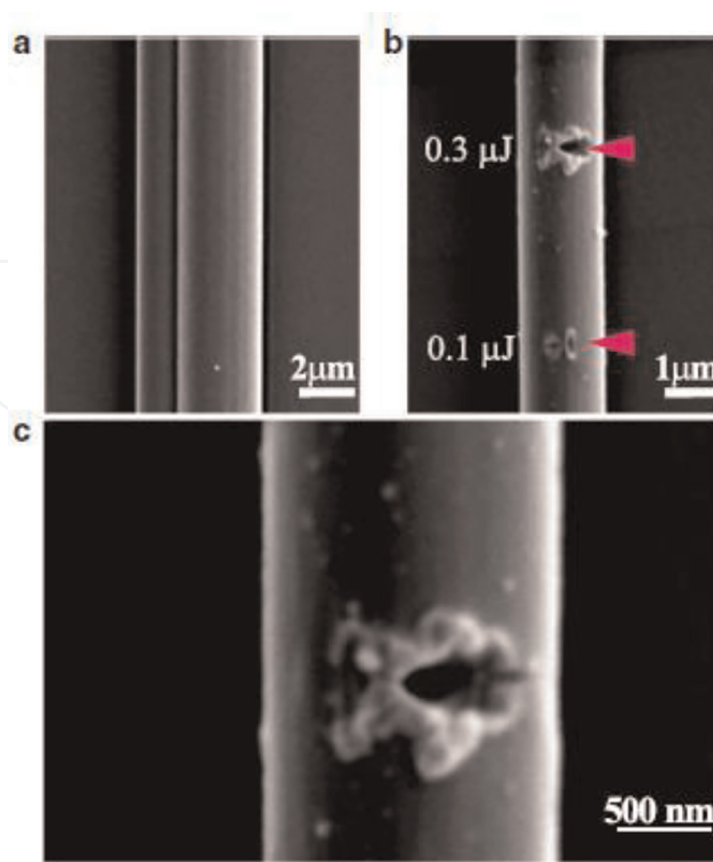


**Figure 17.** (a) Native spider silk. (b) Illustrating ablation of silk fiber at different pulse energies 0.3 and 0.1 μJ, and (c) magnified SEM micrograph illustrating nanoscale ablation of spider silk microfiber at 0.3 μJ [55].

should be possible to further reduce the precision of ablation and may open a route to create nano-patterns on silk for various potential applications.

## 7. Electron beam ablations

Electron beams are used frequently for sterilization, as well as melting and welding metals. A novel e-beam-based material processing technology [58] called electron beam ablation has evolved to perform various surface functionalities. The EBA technique involves an e-beam deflected rapidly over a substrate surface to displace the material in a precisely controlled manner. This results in a textured surface containing an array of protrusions above the original surface and a corresponding array of cavities in the substrate. This process makes it possible to create custom-made, complex surface structures in various materials. The EBA is a complex process that comprises heating, phase change, and removal of a fine fraction from the target surface.

The precursor to this novel material processing technology is e-beam texturing [59]. In this process, the high-energy e-beam flux initially melts and then vaporizes the substrate material. The resulting vapor pressure then leads to the expulsion of molten material to the periphery of the hole. The electromagnetic coils focus the e-beam and then deflect it over the substrate material, leading to a rapid and controlled process. The typical processing speeds are 500–5000 holes per second, and the substrate surface may exhibit re-entrant features. Nowadays, another novel sculpting

technology [59] has come into the picture to replace this texturing process. In this latest advancement, once a molten pool of material has been created, the beam is translated sideways. Under the combined effect of surface tension and vapor pressure, the material from the hole piles up behind the beam, as shown in **Figure 18**. This process is repeated several times at the same or overlapping sites to grow protrusions up to several millimeters accompanied by corresponding intrusions or holes. This technology makes it possible to grow a series of protrusions simultaneously across a substrate.

Careful control of the e-beam process parameters, such as beam accelerating potential, beam current and focus, the pattern design, and precision deflection movements allow for creating a range of different surfaces. These include spikes with a high aspect ratio, burr-free holes, channels, blades, swirls, and networks. It is possible to vary the size, shape, angle of incidence, and distribution of the features to produce customized surfaces within any pattern. Protrusions with dimensions ranging from tens of microns to several millimeters have been created successfully. Moreover, this technology has the flexibility to create a variety of structures, many of which may be impossible to produce using any other processing route. It is performed under a vacuum, thereby avoiding surface contamination. The technology has many potential applications, such as coating of thin films, fabrication of cardiovascular stents, and composite prosthetics. The pulsed-electron beam ablation technique for coating of thin films is described here.

Pulsed-electron beam ablation (PEBA) is an alternative approach that offers numerous advantages over other techniques. For example, for the preparation of thin films, the PEBA approach involves low capital cost, reduced operation/maintenance costs, a small footprint, and relative safety—no toxic gases as in PLA or potential noxious by-products as in solvo thermal routes. PEBA can be a potential candidate for epitaxial growth of high-quality thin films due to significant cost performance advantages, congruent multicomponent film stoichiometry under optimum conditions, process stability, and the scale-up ability for industrial applications.

A typical PEBA system consists of a pulsed-electron beam generator (pulsed-electron beam source), a stainless-steel deposition chamber, target and substrate holders, target and substrate rotating motors, substrate heater, and vacuum system. **Figure 19** shows a simplified schematic of the main pulsed-electron beam chamber components. To operate in pulsed mode, the electron source for high currents is appropriately modified. The channel spark is considered as the most efficient transient hollow cathode (THC) configuration for the generation of electron beams. THC

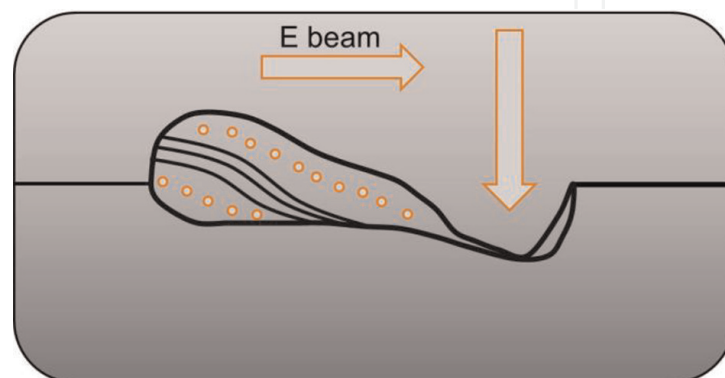


**Figure 18.**  
*Simplified schematic of a PEBA system.*

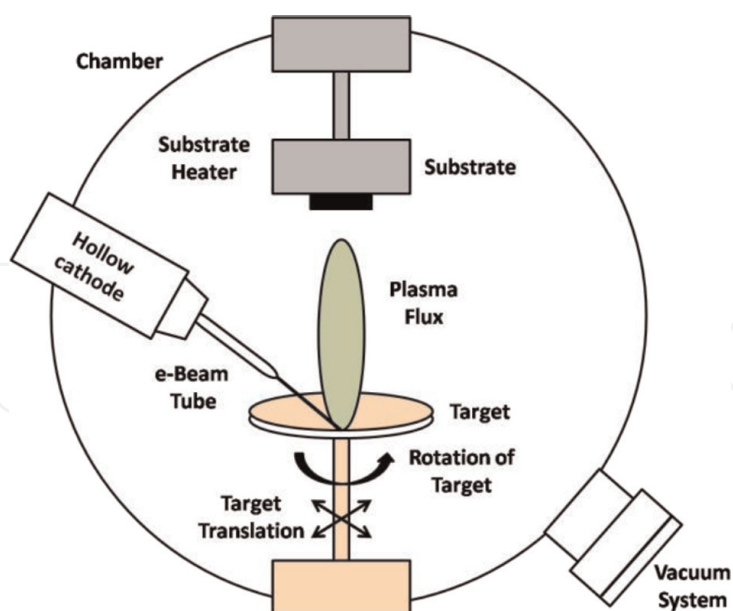


**Figure 19.**  
*Simplified schematic of a PEBA system.*

acts as a low-pressure gas discharge electron source that can produce a focused electron beam with currents up to several kilo-amperes and a pulse duration of  $\sim 100$  ns. Due to the high intensity of the generated beam passing through the deposition chamber, a self-pinch force is developed due to the ionization of background gas by the e-beam. This leads to the formation of a conducting plasma. This self-pinching feature enables the beam propagation, and thus target ablation, inside the deposition chamber without the application of external guiding fields [60, 61].

The triggering of the ablation process is caused by the pulsed-electron beam hitting the target surface. It is the pulsed nature of this technique that enables the confinement of energy within  $1\text{--}2\ \mu\text{m}$  thin subsurface of the target. Such confinement of energy leads to the instantaneous conversion of absorbed energy (energy of electrons) into the heat. The absorption of energy in such a minuscule volume of target material results in a jet evaporation at the target surface. This vapor cloud at the target surface continuously absorbs the majority of the pulsed-electron beam energy, gets ionized, and eventually forms a plasma. A pressure gradient in a direction perpendicular to the surface derives the expansion of the dense plasma which is seen as a plasma-jet (plume). The plasma-plume (high energy species), generated as a result of the interaction of pulsed-electron beam with the target surface, expands in the direction of the maximum pressure gradient at a velocity of about  $10^4$  m/s [62].

It is possible to manipulate ablation spot size, propagation of plume, and its characteristics by variations in the pulsed-electron energy, pressure and chemistry of background gas, and distance between channel spark tube tip and target surface. Plume characteristics and ablation spot size affect other deposition conditions significantly [63]. The production of thin films by PEBA is strongly influenced by the physical parameters in the plume, such as mass distribution, ion and atom velocity, and the angular distribution, of the plume species. Specifically, the homogeneity in film deposition on a substrate and the thickness distribution are determined by the plume shape that evolved during the expansion from the target surface to the substrate. These characteristics are also dependent on the target-substrate distance and the substrate size.



Subsequent to the formation of the plasma plume, the ejected high-energy species impinge on the substrate surface. These energetic species result in the sputtering of some of the surface atoms. A collision region is created between the incident flow and the sputtered atoms. Consequently, a thermalized region is formed that acts as a source for condensation of particles and hence causes the film to grow. Finally, a state of thermal equilibrium is reached, when the condensation rate is higher than the rate of removal of particles by sputtering (**Figure 19**).

## **8. Conclusions**

Direct surface modification techniques using lasers or electron beams are pretty popular due to their reasonable cost and easy adaptation for small and large surfaces with complex geometry. The new generation of low-power femtosecond lasers with unique properties has enhanced the possibility of their use in many new exciting applications. Notably, for the surface modification of polymers, excimer lasers offer great potential. In addition, the medical industry is another sector where laser ablation and electron beam ablation play a key role. The medical industry has an ever-growing demand for the surfaces of implants and stents to enhance their performance. The technological advancements in e-beam ablation have resulted in the development of a novel surface processing technique capable of addressing these needs by rapidly producing bespoke surface features in a clean environment. It is being investigated for a range of medical applications.

## **Acknowledgements**

The authors acknowledge the support from Electron Microscopy & Nanoscience Laboratory, Department of Soil Science, Punjab Agricultural University, Ludhiana. The authors also acknowledge Dr. Kamal P. Singh from the femtosecond laser lab, Physical Sciences, IISER Mohali, INDIA for his kind contribution in Z-scan and multiphoton analysis work on single fiber.

## **Conflict of interest**

The authors declare no conflict of interest.

IntechOpen


## Author details

Mehra S. Sidhu\* and Nitish Dhingra  
Department of Soil Science, Electron Microscopy and Nanoscience Laboratory,  
Punjab Agricultural University, Ludhiana, India

\*Address all correspondence to: [sidhums@pau.edu](mailto:sidhums@pau.edu)

## IntechOpen

---

© 2022 The Author(s). Licensee IntechOpen. This chapter is distributed under the terms of the Creative Commons Attribution License (<http://creativecommons.org/licenses/by/3.0>), which permits unrestricted use, distribution, and reproduction in any medium, provided the original work is properly cited. 

## References

- [1] Iordanova E, Yankov G, Garasz K. Surface modification of different materials by fs-laser irradiation. *Bulgarian Journal of Physics*. 2017;**44**:133
- [2] Schwibbert K, Menzel F, Epperlein N, Bonse J, Krüger J. Bacterial adhesion on femtosecond laser-modified polyethylene. *Materials*. 2019;**12**:3107
- [3] Xue X, Lu L, Wang Z, Li Y, Guan YC. Improving tribological behavior of laser textured Ti-20Zr-10Nb-4Ta alloy with dimple surface. *Materials Letters*. 2021; **305**:130876
- [4] Liu Y, Yuan G, Guo C, Ngo C-V, Li W. Femtosecond laser fabrication and chemical coating of anti-corrosion ethylene-glycol repellent aluminum surfaces. *Materials Letters*. 2022;**323**: 132562
- [5] Jiao L, Chua ZY, Moon SK, Song J, Bi G, Zheng HY. Femtosecond laser produced hydrophobic hierarchical structures on additive manufacturing parts. *Nanomaterials*. 2018;**8**:601
- [6] Jalil SA, Akram M, Bhat JA, Hayes JJ, Singh SC, Kabbash ME, et al. Creating superhydrophobic and antibacterial surfaces on gold by femtosecond laser pulses. *Applied Surface Science*. 2020; **506**:144952
- [7] Sun H, Han M, Niemz MH, Bille JF. Femtosecond laser corneal ablation threshold: Dependence on tissue depth and laser pulse width. *Lasers in Surgery and Medicine*. 2007;**39**:654
- [8] Olivié, G., Giguère, D., Vidal, F., Ozaki, T., Kieffer, J. C., Nada, O., and Brunette I., Wavelength dependence of femtosecond laser ablation threshold of corneal stroma, *Optic Express* 16, 4121 (2008).
- [9] Vogel A, Noack J, Huttman G, Paltauf G. Mechanisms of femtosecond laser nanosurgery of cells and tissues. *Applied Physics B*. 2005;**81**:1015
- [10] Perry MD, Stuart BC, Banks PS, Feit MD, Yanovsky V, Rubenchik AM. Ultrashort-pulse laser machining of dielectric materials. *Journal of Applied Physics*. 1999;**85**(9):6803-6810
- [11] Hoerauf H, Brix A, Winkler J, Droege G, Winter C, Birngruber R, et al. Photoablation of inner limiting membrane and inner retinal layers using the erbium: YAG-laser: An in vitro study. *Lasers in Surgery and Medicine*. 2006;**38**: 52-61
- [12] Yu PK, Miller J, Cringle JS, Yu D-Y. Experimental retinal ablation using a fourth-harmonic 266 nm laser coupled with an optical fiber probe. *Investigative Ophthalmology & Visual Science*. 2006; **47**:1587-1593
- [13] Zysset B, Fujimoto JG, Deutsch TF. Time- resolved measurement of picosecond optical breakdown. *Applied Physics B: Lasers and Optics*. 1989;**48**(2): 139-147
- [14] Perry MD, Campbell EM. Petawatt Laser Proposal, LLNL Internal Report –1992. Anaheim, CA: Conference on Lasers and Electro-Optics; 1993
- [15] Du D, Liu X, Squier J, Korn G, Mourou G. Laser-induced breakdown by impact ionization in SiO<sub>2</sub> with pulse widths from 7 ns to 150 fs. *Applied Physics Letters*. 1994;**64**:3071-3073
- [16] Stuart BC, Feit MD, Rubenchik AM, Shore BW, Perry MD. Laser- induced damage in dielectrics with nanosecond and sub picoseconds pulses. *Physical Review Letters*. 1995;**74**:2248-2251

- [17] Pronko PP, VanRompay P, Horvath A, Loesel CF, Juhasz T, Liu X, et al. Avalanche ionization and dielectric breakdown in silicon with ultrafast laser pulses. *Physical Review B*. 1998;**58**: 2387-2390
- [18] Niemz MH. *Laser—Tissue Interactions*. 3rd ed. USA: Springer Inc; 2007
- [19] Vogel A, Venugopalan V. Mechanisms of pulsed laser ablation of biological tissues. *Chemical Reviews*. 2003, 2003;**103**:577-644
- [20] Sidhu MS, Kumar B, Singh KP. The processing and heterostructuring of silk with light. *Nature Materials*. 2017;**11**: 938-945
- [21] Kaiser A, Rethfeld B, Vicane M, Simon G. Microscopic processes in dielectrics under irradiation by subpicosecond laser pulses. *Physical Review B*. 2000;**61**:11437-11450
- [22] Wong K, Vongehr S, Kresin VV. Work functions, ionization potentials, and in between: Scaling relations based on the image-charge model. *Physical Review B*. 2003;**67**:035406-035414
- [23] Stuart BC, Feit MD, Herman S, Rubenchik AM, Shore BW, Perry MD. Nanosecond-to-femtosecond laser-induced breakdown in dielectrics. *Physical Review B*. 1996;**53**:1749-1761
- [24] Il'insky YA, Keldysch KA. *Electromagnetic Response of Material Media*. New York, USA: Plenum; 1994
- [25] Liu X, Du D, Mourou G. Laser ablation and micromachining with ultrafast laser pulse. *IEEE Journal of Quantum Electronics*. 1997;**33**:1706-1716
- [26] Manenkov AA. Ultimate laser intensities in transparent solids. *Laser Physics*. 1996;**6**(3):501-505
- [27] Keldysh LV. Ionization In The Field Of A Strong Electromagnetic Wave. *Soviet Physics JETP*. 1965;**20**:1307-1314
- [28] Shen N. *Photo-Disruption of Biological Tissues Using Femtosecond Laser Pulses* [PhD thesis]. Harvard University, USA; 2003
- [29] Yust BG, Mimun LC, Sardar DK. Optical absorption and scattering of bovine cornea, lens and retina in near infrared region. *Lasers in Medical Science*. 2011;**27**(2):413-422
- [30] Hanczyc P, Samoc M, Norden B. Multiphoton absorption in amyloid protein fibres. *Nature Photonics*. 2013;**7**: 969-972
- [31] Applegate MB, Marelli B, Kaplan DL, Omenetto FG. Determination of multiphoton absorption of silk fibroin using the Z-scan technique. *Optics Express*. 2013;**21**:29637-29642
- [32] Sidhu MS. *Parametric study of femtosecond laser-assisted selective removal of neovascular structures in animal eye*. University of Science and Technology. [PhD thesis]. 2014
- [33] Brooks BJ, Ambati BK, Marcus DM, Ratanasit A. Photodynamic therapy for corneal neovascularisation and lipid degeneration. *The British Journal of Ophthalmology*. 2004;**88**:840
- [34] Mita M, Kanamori T, Tomita M. Corneal heat scar caused by photodynamic therapy performed through an implanted corneal inlay. *Journal of Cataract & Refractive Surgery*. 2013;**39**:1768-1773
- [35] Holzer MP, Solomon KD, Vroman DT, Sandoval HP, Margaron P, Kasper TJ, et al. Photodynamic therapy with verteporfin in a rabbit model of corneal

neovascularization. *Investigative Ophthalmology & Visual Science*. 2003; **44**(7):2954-2958

[36] Kulkarni GR. Laser-tissue interaction studies for medicine. *The Bulletin of Materials Science*. 1988;**11**: 239-244

[37] Schatz H, Madeira D, McDonald HR, Johnson RN. Progressive enlargement of laser scars following grid laser photocoagulation for diffuse diabetic macular edema. *Archives of Ophthalmology*. 1991;**109**(11):1549-1551

[38] Xu YG, Xu YS, Huang C, Feng Y, Li Y, Wang W. Development of a rabbit corneal equivalent using an acellular corneal matrix of a porcine substrate. *Molecular Vision*. 2008;**14**:2180-2218

[39] Welch AJ, van Gemert MJC. *Optical Thermal Response of Laser-Irradiated Tissue*. New York, USA: Plenum Press; 1995

[40] Venugopalan V, Nishioka NS, Mikic' BB. Thermodynamic response of soft biological tissues to pulsed infrared laser irradiation. *Biophysical Journal*. 1996;**70**: 2981-2993

[41] Schaffer CB, Nishimura N, Glezer EN, Kim AM-T, Mazur E. Dynamics of femtosecond laser-induced breakdown in water from femtoseconds to microseconds. *Optics Express*. 2002;**10**:196-203

[42] Kennedy PK, Boppart SA, Hammer DX, Rockwell BA, Noojin GD, Roach WP. A first-order model for computation of laser-induced breakdown thresholds in ocular and aqueous media. Part II: Comparison to experiment. *IEEE Journal of Quantum Electronics*. 1995;**31**:2250-2257

[43] Vogel A, Noack J, Nahen K, Theisen D, Busch S, Parltitz U, et al. *Energy*

balance of optical breakdown in water at nanosecond to femtosecond time scales. *Applied Physics B: Lasers and Optics*. 1999;**68**:271-280

[44] Hammer DX, Frenz M, Jansen ED, Thomas RJ, Noojin GD, Rockwell BA, et al. Shielding effectiveness of laser-induced breakdown in water for pulse durations from 5 ns to 125 fs. *Applied Optics*. 1997;**36**:5630-5640

[45] Sidhu MS, Woo SY, Kim WK, Lee HS, Yahng JS, Kim KJ, et al. Optoperforations of retinal blood vessels in an intact porcine eye by using a femtosecond laser assisted microsurgery system. *Journal of the Korean Physical Society*. 2011;**58**(6):1605-1613

[46] Sidhu MS, Kim EK, Woo S-Y, Song MC, Jeoung SC, Park Y-I. Femtosecond-laser-assisted optoperforation of the primary retinal blood vessels and the retina tissue of porcine eyes. *The Journal of the Korean Physical Society*. 2009;**55**: 467-476

[47] Schaffer CB, Jamison AO, Garcia JF, Mazur E. *Ultrafast Lasers: Technology and Applications*. New York: Marcel Dekker Inc; 2002. p. 395

[48] Vogel A, Noack J, Huttman G, Paltauf G. Mechanism of femtosecond laser nanosurgery of cells and tissues. *Applied Physics B*. 2005;**81**(8):1015-1047

[49] Yoon TO, Shin HJ, Jeoung SC, Park YI. Formation of superhydrophobic poly (dimethylsiloxane) by ultrafast laser-induced surface modification. *Optics Express*. 2008;**16**(17):12715-12725

[50] Sidhu MS, Choi MY, Woo SY, et al. Femtosecond laser-assisted selective reduction of neovascularization in rat cornea. *Lasers in Medical Science*. 2014; **29**:1417-1427

- [51] Vogel A. Nonlinear absorption: Intraocular microsurgery and laser lithotripsy. *Physics in Medicine and Biology*. 1997;**42**(5):895-912
- [52] Vogel A, Noack A, Nahen K, Theisen D, Birngruber R, Hammer DX, et al. Laser-induced breakdown in the eye at pulse durations from 80 ns to 100 fs. *Proceedings of SPIE*. 1998;**3255**:34-49
- [53] Sawa M, Awazu K, Takahashi T, Sakaguchi H, Horiike H, Ohji M, et al. Application of femtosecond ultrashort pulse laser to photodynamic therapy mediated by indocyanine green. *The British Journal of Ophthalmology*. 2004;**88**:826-831
- [54] Giguère D, Olivie G, Vidal F, Toetsch S, Girard G, Ozaki T, et al. Laser ablation threshold dependence on pulse duration for fused silica and corneal tissues: Experiments and modeling. *Journal of the Optical Society of America. A*. 2007;**24**: 1562-1568
- [55] Sidhu MS, Singh KP. Ablation of silicon and ultrathin fibers using single femtosecond pulse. *Indian Journal of Physics*. 2019;**93**:1619. DOI: 10.1007/s12648-019-01419-5
- [56] Vollrath F, Madsen B, Shao Z. The effect of spinning conditions on the mechanics of a spider's dragline silk. *Proceedings of the Royal Society of London B*. 2001;**268**:2339
- [57] Preuss S, Demchuk A, Stuke M. Sub-picosecond UV laser ablation of metals. *Applied Physics A: Materials Science & Processing*. 1995;**61**:33
- [58] B.G.I. Dance and E.J.C. Kellar (Inventors) Workpiece Structure Modification, Surfi-Sculpt, International Patent Publication Number WO 2004/028731 A1 Applicant: The Welding Institute.
- [59] B.G.I. Dance (Inventor). 'Modulated Surface Modification,' International Patent Publication Number WO 2002/094497 A3, Applicant: The Welding Institute
- [60] Buxton AL, Dance BGI. Surfi-Sculpt – revolutionary surface processing with an electron beam. In *Proceedings of 4th International Surface Engineering Congress*, 1–3 August, St. Paul, Minnesota, USA. 2005. pp. 107-110. ISBN: 0-87170-835-3
- [61] Fernsler RF, Hubbard RF, Lampe M. *Pinched Propagation of High-power, Pulsed Electron Beams for Welding and Materials Processing Applications*. Washington DC: Naval Research Lab; 1994. pp. 1-59
- [62] Nistor M, Gherendi F, Mandache NB. Fast imaging of ablation plasma produced by a pulsed electron beam. *Journal of Transactions on Plasma Science*. 2011;**39**:2800-2801
- [63] Christen HM, Lee DF, List FA, Cook SW, Leonard KJ, Heatherly L, et al. Pulsed electron deposition of fluorine based precursors for  $\text{YBa}_2\text{Cu}_3\text{O}_{7-x}$ -coated conductors. *Journal of Superconductor Science and Technology*. 2005;**18**:1168